Investigation of an alternative spatial discretizaiton for the Fokker-Planck equation

by

Julian Rabbie

to obtain the degree of Bachelor of Science
at the Delft University of Technology,
to be defended publicly on August 5, 2016 at 10:00 AM.

Student number:	4307720	
Project duration:	April 18, 2016 – August 5, 2016	
Thesis committee:	Dr. ir. D. Lathouwers,	TU Delft, supervisor
	Prof. dr. ir. J. L. Kloosterman,	TU Delft

An electronic version of this thesis is available at `http://repository.tudelft.nl/`.

TU Delft Delft University of Technology

Abstract

Proton therapy is a relatively new way of using elementary particles to treat cancer. The main benefit of this kind of radiotherapy is however also its downside; protons deposit a big percentage of their initial energy on a relatively small volume. This causes the destruction of either targeted tumor cells or the surrounding healthy cells. To minimize the amount of damage done to healthy tissue, there is need for a method that determines the initial parameters of a proton beam used in radiotherapy as accurate as possible while requiring the least computational power.

The central equation used in this thesis to describe the behavior of proton transport is the Fokker-Planck equation. This equation is numerically solved by using the linear discontinuous Galerkin method. This is a very accurate method for solving partial differential equations like the Fokker-Planck equation. To use the discontinuous Galerkin method, all variable domains are split into finite elements and a system of coupled equations is formed and solved to reach a numerical approximation of the amount of particles on every surface.

The main question in this thesis is how the level of convergence depends on the amount of elements used. To analyze this dependence, the quantitative error is determined for a certain number of either spatial or energy elements. The error is determined for two separate cases: one where the slope is linear on every spatial domain and one where the slope is constant. The use of a constant slope on every domain causes the total number of equations to be solved per energy and spatial element to decrease. If there is no significant accuracy loss while using a constant slope, this method could be used in further research, to ultimately reach a method that solves the proton beam parameters with high accuracy and low computational time.

Our results show that a choice of boundary condition causes a loss of accuracy in the energy domain, while the choice of spatial discretization induces a loss in accuracy in the spatial domain. The results are generated by setting either the number of spatial elements or energy groups to a certain value, while varying the other. We concluded that the choice of the number of elements which is held constant also influences the convergence. Space and energy seem to be coupled to a certain extent and further research is needed to draw concrete conclusions about the effect of the choice of spatial discretization for a case in which actual dose distribution calculations are made.

Contents

1

Proton therapy as cancer treatment

According to the World Health Organization, cancer is still the leading cause of death worldwide. Since there is no vaccination (yet) to prevent cancer from ever occurring, researchers of all kinds of fields are working together to improve today's available treatments. The most common types of treatments are (a combination of) the surgical removal of the tumor(s), chemotherapy, immunotherapy and radiotherapy. In this thesis we will focus on the latter.

1.1. Radiotherapy

Radiotherapy is the use of subatomic particles to destroy tumor cells. The main benefit of radiotherapy is however also its biggest downside: the destruction of cells. Not only the dangerous tumor cells are affected, but also the healthy tissue surrounding it. To indicate the level of energy deposited per tissue mass, the term *absorbed dose* is used. In the ideal case, the absorbed dose is 100% for the tumor cells and 0% for the surrounding healthy tissues. Sadly this is not possible in reality, since there will always be uncertainties due to the stochastic behavior of elementary particles and also in the exact position of the tumor, due to breathing and a variety of small movements. Although improvements are made in reducing these uncertainties, like the usage of MRI instead of CT scans for the imaging of the tumor inside the body, researchers are still looking to improve the so called *therapeutic ratio*. This ratio is defined as the proportion of dose delivered to the targeted (tumor) tissue relative to the surrounding tissue.

1.1.1. Photon therapy

Aside from improving the imaging, other big improvements can be made on the used particles to improve the therapeutic ratio. The most commonly used form of radiotherapy uses photons (X-rays) to deliver enough energy to the tumor cells to destroy them. Because photons have no mass nor charge, they deposit their energy in a way that is not optimal for cancer treatment. The peak in energy deposition is reached when the photons have traveled just a few centimeters in the human tissue, so especially tumors that are positioned relatively deep inside a body are hard to irradiate without severely damaging the surrounding healthy tissue. The damage inflicted to the healthy tissue could cause cell mutation, new tumors and in some cases radiation sickness.

1.1.2. Proton therapy

Since a few decades there is a new kind of radiotherapy available that uses protons instead of photons. A small particle accelerator is used to give the protons kinetic energy with which they are transported to the tissue. The main benefit of using protons is the way these particles deposit their energy. This is done in a typical kind of way, which results in a so called *Bragg peak* in the absorbed dose at a certain depth. This is illustrated in figure 1.1.The Bragg peak causes the protons to deposit most of their energy at a certain depth, which can be modified by altering the initial kinetic energy of the protons. This effect occurs because protons have a relatively large mass, which causes them to travel in a straight line through matter with a small level of interaction. As the protons travel through matter, they interact with the electrons of the atoms of the material, which causes the protons to slow down. When a certain speed (energy) is reached, the protons move slow enough to collide with other bigger particles.

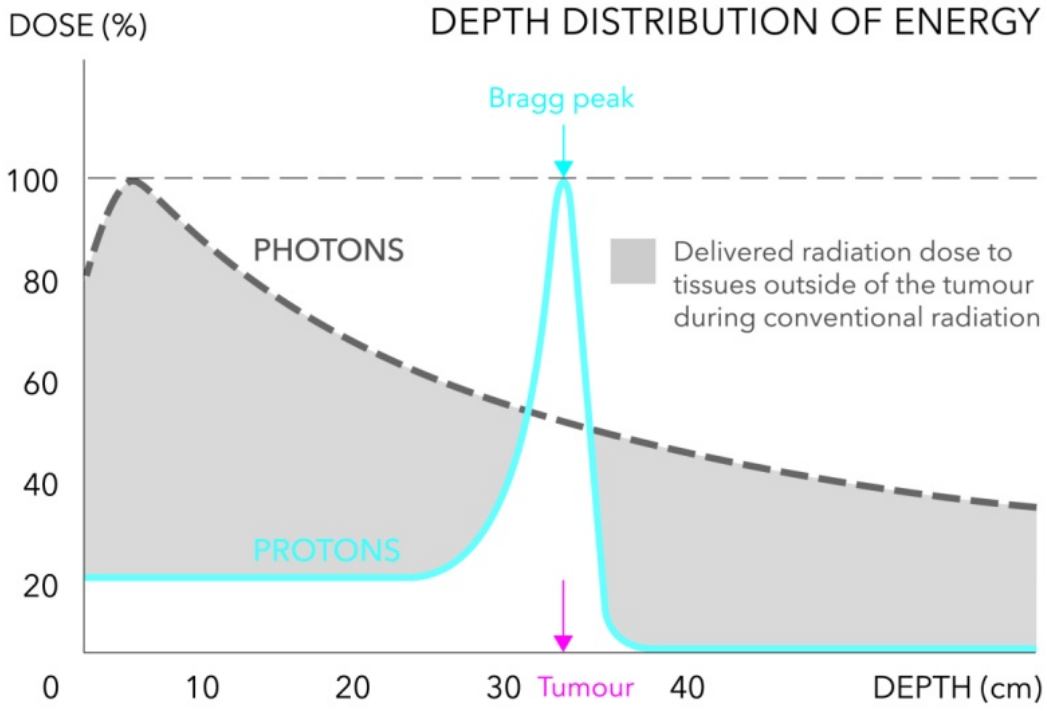

Figure 1.1: *The dose distribution of protons vs. photons for a tumor at a depth of around 30 cm (Proton Therapy Center, 2012)*

The sudden rise of interactions causes the Bragg peak in the delivered dose.
Because of this specific property, a much smaller area can be targeted more accurately with a higher dose by a proton beam than by using ionizing radiation, while the surrounding tissue receives a significantly smaller dose. More than half a century ago Wilson (1946) wrote the first paper about the theory behind radiation therapy using protons. A decade later the first treatments were carried out in the United States and Sweden using particle accelerators which were mainly used for physics research. These treatments turned out to be successful and over the next 60 years, almost 120.000 patients were treated by using proton radiotherapy (Jermann, 2015). At the moment there are treatment centers that use protons to treat cancer all over the world, mainly in Germany, Japan and the United States. Next to the Reactor Institute Delft, on the campus of the University of Delft, the first proton therapy center of the Netherlands is built, which will be officially opened in 2017. This is a joint initiative of Leiden UMC, Erasmus MC and the TU Delft and about 600 patients will be able to be treated yearly.

1.2. Dose calculation

Since every tumor and patient is different, the parameters for the proton beam must be determined every time a new patient will be treated. In general there are three methods of determining these parameters. An overview of these methods is given in table 1.1.

Table 1.1: *An overview of the three main methods of determining proton beam paramters*

	Computational cost	Accuracy
Fermi pencil beam	*Low*	Medium
Monte Carlo simulations	**High**	**High**
Numerical solving of the Fokker-Planck equation	Medium	**High**

The easiest way of determining the particle beam parameters is by using the Fermi pencil beam approximation. This can be described as a particle beam that starts from a single point from where it diverges in a cone-like shape. The initial parameters are calculated by starting with the linear Boltzmann equation and

using the Fokker-Planck approximation. From here the equation is analytically solved using the Fermi-Eyges formula, which gives an exact solution. In practice, these parameters can be calculated in the order of seconds, so the computational cost is very low. The accuracy of this approximation is not optimal however. For tumors that are surrounded by inhomogeneous tissue, so where the protons have to travel through materials that have significant differences in density and scatter properties, a certain amount of protons will not give off their energy at the targeted tissue, but somewhere else. This is also a problem for tumors that lie in an area like the brain, where the density differences might not be significant, but any damage to healthy tissue that surrounds the tumor can cause severe damage. The main benefit of the way protons deposit their energy in a material, the Bragg peak, is a big downside in these cases, since the protons will distribute a big portion of their energy onto healthy tissue, if the accuracy of the beam is not high enough.

A solution for this problem could be the use of Monte Carlo simulations. These simulations make use of known probability distributions, so in this case those of charged particles, to statistically describe the average behavior of the particles. As the uncertainty of these simulations is proportional to the inverse square root of the total number of particles that are taken into account, this method can get as accurate as we want. However, the more particles we take into account, the longer it takes to finish the simulations. In practice Monte Carlo simulations take too long to be practically applicable. The simulations can be used as benchmark cases however, to test the accuracy of other methods.

The third way is the numerical solving of the Fokker-Planck equation by using accurate numerical approximation. A wide variety of numerical approximations can be used and are tested (Uilkema, 2012), but in this thesis we will solely use the discontinuous Galerkin method. In chapter 3 we will further describe this method. Most numerical methods for solving differential equations rely on the finite element method (FEM). For a numerical solution to converge to the actual smooth solution, a sufficient number of cells are needed for all variables. The number of cells needed for reaching an accurate solution is dependent on the numerical method used, so the goal is to find a numerical method that requires the least computational time combined with a high level of accuracy. The method that could be improved by the work done in this thesis can determine the dose distribution in a few hours. This is still relatively time consuming for practical use, so any significant improvements made on this method may enable it to become a widely used way of determining the parameters.

1.3. Goals of this thesis

The main goal of this thesis is determining whether a simplification in a certain discretization has a significant negative impact on the accuracy of the dose calculations. If this is not the case, the simplification can be implemented in future work which could result in a method for determining the initial beam parameters with low computational cost and a high accuracy.

We will start with describing the main equation for proton transport, called the Boltzmann transport equation. A few simplifications will be made to this equation to make it easier numerically solvable. In the following chapter the used numerical methods and discretizations are described, together with a more specific formulation of the main question of this thesis. At the end of this chapter we will end up with a set of equations, which are solved with a computer by using a LAPACK routine. The results will be displayed in chapter 4. Finally, we discuss the most important conclusions we can determine with these results and how these could be used in future work. This report is part of the thesis research of the bachelor Applied Physics at the Technology University of Delft.

2

The proton transport equation

In 1872 Ludwig Boltzmann formulated an equation that describes the statistical behavior of particles in a system that is not in thermal equilibrium. Since a physically realistic system contains a large number of particles, Boltzmann chose to describe the positions and velocities on a macroscopic level instead of considering every individual particle by using a probability density function as main quantity. He stated that this probability density function changes over time due to a possible external force field, the streaming of the particles and the collisions they undergo as they travel through a medium.

2.1. Transport equation in three spatial dimensions

In this thesis we describe the properties of charged elementary particles traveling through a medium using a quantity φ, the angular flux. This can be seen as the number of particles that travel through a surface at a point in time, so the units of the angular flux are $[cm^{-2}s^{-1}]$. One could also choose to describe the properties of the protons using a probability distribution, but since we are interested in quantitative values these are not interesting in this research. We will look at a steady-state situation with the absence of external forces, in which the angular flux is given by equation 2.1 (James J. Duderstadt, 1976).

$$\hat{\boldsymbol{\Omega}} \cdot \nabla \varphi(\boldsymbol{r}, E, \hat{\boldsymbol{\Omega}}) + \sigma_t(\boldsymbol{r}, E)\varphi(\boldsymbol{r}, E, \hat{\boldsymbol{\Omega}}) = \int_{4\pi} d\hat{\boldsymbol{\Omega}}' \int_0^\infty dE' \sigma_s(E' \to E, \hat{\boldsymbol{\Omega}} \to \hat{\boldsymbol{\Omega}}')\varphi(\boldsymbol{r}, E, \hat{\boldsymbol{\Omega}}) + s(\boldsymbol{r}, E, \hat{\boldsymbol{\Omega}}) \tag{2.1}$$

This equation is known as the *Boltzmann transport equation.* It can be used in a number of fields, like in the transportation of neutrons in a nuclear reactor, but we will use it to describe the motion of protons and thus we will refer to it as the *proton transport equation.* As mentioned earlier, the main quantity in this equation is the angular flux φ, which is a function of the particle position $\boldsymbol{r}$, its energy E and direction vector $\hat{\boldsymbol{\Omega}}$. There are four terms to be analyzed in this equation, which we will describe separately.

The first term on the left hand side (LHS) is referred to as the streaming term, which is the part of the Boltzmann equation that describes the streaming of the particles as they travel through a medium. The second term on the LHS is called the total removal term, where σ_t is the total macroscopic cross section. In elementary particle transport physics, the cross section is the characterization of the probability that a particle will collide with a nucleon of the medium in which it is located per unit length traveled. These collisions can occur due to a number of different reasons and σ_t is the sum of all these cross sections, thus this term describes total 'removal' of particles.

The first term on the right hand side (RHS) describes the scattering of particles with energy E' and angle Ω' to the energy E and angle Ω that are considered in the angular flux and is known as the Boltzmann scattering operator. σ_s is therefore the cross section of solely scattering collisions. The last term, $s(\boldsymbol{r}, E, \hat{\boldsymbol{\Omega}})$, is introduced to this balance equation to take any source of the considered particles inside the domain into account. In this thesis we will only look at situations where there is no source of particles inside the domain, but only on the boundaries.

2.2. Transport equation in one spatial dimension

Since the research which is done in this thesis mainly focuses on the numerical solution of an equation, we will make some more simplifications to equation 2.1 to make the numerical methods easier to implement in the time window that is available for this thesis. In this section we will describe how the transport equation changes under the transformation from a 3-dimensional spatial domain to a 1-dimensional domain.

First of all, the spatial variable $\boldsymbol{r}$ becomes an arbitrary 1-dimensional spatial variable x. This means that the streaming term reduces to

$$\hat{\boldsymbol{\Omega}} \cdot \nabla \varphi(x,E,\theta) = \left(\Omega_x \frac{\partial}{\partial x} + \Omega_y \frac{\partial}{\partial y} + \Omega_z \frac{\partial}{\partial z}\right)\varphi(x,E,\theta) = \Omega_x \frac{\partial \varphi(x,E,\theta)}{\partial x} = \mu \frac{\partial \varphi(x,E,\theta)}{\partial x}$$

With $\mu \equiv \Omega_x = \cos(\theta)$, the cosine of the scattering angle. Since the scattering angle for this 1-dimensional spatial domain can only be 0 or π, we define μ to be -1 for transport from right to left and 1 for transport from left to right. We choose to always have the latter kind of transport, so from here on we will define $\mu = 1$ and it will therefore not be considered in the remainder of this thesis. Since we are also only interested in effects of space and energy dependence of φ, we will no longer write it as function of the angle θ. Using this simplification, we get the following resulting equation:

$$\frac{\partial \varphi(x,E)}{\partial x} + \sigma_t \varphi(x,E) = L_B(E)\varphi(x,E) \tag{2.2}$$

Where L_B is the Boltzmann scatter operator, which is the same as the first term on the right in 2.1. This operator is only a function of energy. In the next section, we will make use of the Fokker-Planck approximation to come to the most important equation of this thesis.

2.3. The Fokker-Planck approximation

The Fokker-Planck equation, surprisingly first introduced by Kolmogoroff (1931), is named after Adriaan Fokker and Max Planck for their extensive research on its implications. It describes the change of the probability density function of the velocity of a particle over time, under the influence of drag and stochastic forces. The same ideas that Kolmogoroff used to derive the Fokker-Planck equation, can be adapted to approximate the Boltzmann scatter operator, thus it is referred to as the Fokker-Planck approximation.

The term on the RHS in equation 2.2 is called the Boltzmann scatter operator and describes the influence of scattering collisions of the protons with nucleons. This can be split into two terms, one that considers elastic collisions into account and one that describes the contribution of inelastic collisions. Using a Taylor expansion and under the assumption that the protons collide a larger number of times without losing a significant amount of energy, Uilkema (2012) rewrote this term into

$$L_B(E)\varphi(x,E) \approx \frac{\partial S(E)\varphi(x,E)}{\partial E} + \frac{1}{2}\frac{\partial^2 T(E)\varphi(x,E)}{\partial^2 E}$$

Where the first term on the RHS is called the continuous slowing down (CSD) operator and the second term is called the energy straggling operator. The CSD operator can be physically interpreted as the continuous transfer of energy from the protons to the atomic electrons due to inelastic collisions. The energy straggling operator can be seen as the term that takes the collisions due to the stochastic properties of the protons into account. The coefficients $S(E)$ and $T(E)$ are called the stopping power and the energy straggling respectively. The values of these coefficients can be obtained by using analytical approximations for these functions or they can be determined experimentally. Especially the CSD operator is very important for describing the transport of protons, since this is the operator that mainly causes the Bragg peak. The contribution of the energy straggling is relatively small however, so in this thesis it will be ignored. The result of the previous sections can be combined to give a final resulting equation, known as the **Boltzmann-Fokker-Planck equation**, which we will numerical solve in the next chapter.

$$\boxed{\frac{\partial \varphi(x,E)}{\partial x} + \sigma_t \varphi(x,E) - \frac{\partial S(E)\varphi(x,E)}{\partial E} = 0} \tag{2.3}$$

3

Numerical approach

3.1. The Galerkin method

To solve equation 2.3 numerically, we use the **linear discontinuous Galerkin method**. This is a very accurate way of projecting an actual solution onto polynomials using discontinuous finite elements. The Galerkin method enables an equation to be rewritten into a weak formulation containing multiple coupled equations, which are (easier) solvable. These equations can be written as a matrix system, which we will solve in our code. The result can be plotted and compared with a reference solution. We will first explain how the Galerkin method works and how each term in 2.3 is treated. Finally, we will combine all these steps to get to the total matrix system we need to solve.

3.1.1. The Galerkin method

The Galerkin method is based on Ritz's method, which is a method for solving partial differential equations (PDE's) like 2.3 (van Kan et al., 2005). Ritz's method is based on the assumption that the solution of a PDE, $f(x)$, can be written as a linear combination of *basis functions*. The Galerkin method is an expansion of this method and solves a PDE by taking the next steps

1. Choose n basis functions: $b_1(x), b_2(x), \ldots, b_n(x)$, with $Lf(x) = b_k(x)$ (where L is a linear operator).

2. Rewrite the solution $f(x)$ as a linear combination of the basis functions for each element k: $f^k(x) = \sum_{i=1}^{n} c_i^k b_i^k(x)$.

3. Multiply the equation with a test function $u(x)$ and integrate over a single element. The Galerkin method uses one of the basis functions as test function ($u(x) = b_j(x)$).

4. Repeat the third step for every basis function to get a system of n equations.

The resulting set of equations can be represented by the following matrix system

$$\boldsymbol{Ax} = \boldsymbol{b} \tag{3.1}$$

Where A is a $n \times n$ matrix system, x is the vector containing the coefficients $c_1, c_2, \ldots, c_n$ and b a vector containing the constants of each equation.

3.2. Discretization and basis functions

Because the size of the matrix A in 3.1 depends on the number of basis functions, we need to make a choice between accuracy and computing time. Since 2.3 only contains first order terms we can reach accurate results by using basis functions which are also first order. This linearity combined with the discontinuity on the boundaries, allows us to reach an sufficiently accurate solution for 2.3 by using two basis functions for both spatial and energy discretizaiton.

3.2.1. Space

For our spatial discretization, we use two linear basis functions, which we will call $h_1(x)$ and $h_2(x)$. These are defined on element k as follows

$$h_{1,k}(x) = 1 - \frac{(x - x_l)}{\Delta x} \tag{3.2}$$

$$h_{2,k}(x) = 1 + \frac{(x - x_r)}{\Delta x} = 1 - h_{1,k}(x) \tag{3.3}$$

Where x_l and x_r are the spatial coordinates of the left and right boundary of an element respectively and Δx is the width of one element. With a linear combination of these basis functions, one can determine the linear projection of the actual solution. If the solution is not smooth or the width of the spatial elements is too big, the linear approximation might have trouble converging to the actual solution. We will analyze the error between the numerical solution and a reference solution to determine the effect of the spatial cell width on the convergence. Our total spatial domain is chosen to be 8 cm long ($L = 8$).

3.2.2. Energy

To discretize our energy domain, we split the energies into so called energy groups with equal width ΔE, a method commonly used in finding numerical solutions of particle transport equations. We mostly choose this width to be equal for every group, but in case we need to focus on particles with a specific energy, we can set the width of these groups to a smaller value. As basis functions for the Galerkin method we treat the slope and average in each group separately. The basis functions are defined as

$$p^A = 1 \tag{3.4}$$

$$p_g^E(E) = \frac{2}{\Delta E}(E - E_g) \tag{3.5}$$

Where E_g is the middle of the energy group, p^A is the basis function that describes the average and p^E the slope of the linear approximation of the flux within a group. Note that $p_g^E(E)$ is a function of the considered energy group, while p^A is not. These functions are scaled Legendre polynomials, which have a convenient orthogonality property:

$$\int_{E_{g+\frac{1}{2}}}^{E_{g-\frac{1}{2}}} p^i(E) p^j(E) dE = \frac{\Delta E}{2j+1} \delta_{ij} \tag{3.6}$$

With δ_{ij} the Kronecker delta function, which is 1 if $i = j$ and 0 in all other cases. Because of this orthogonality, all cross-multiplication terms will cancel when applying the Galerkin method. Again, the solution needs to be smooth and the number of groups must be large enough for the numerical solution to converge to the analytical solution.
All four test functions are illustrated in figure 3.1.

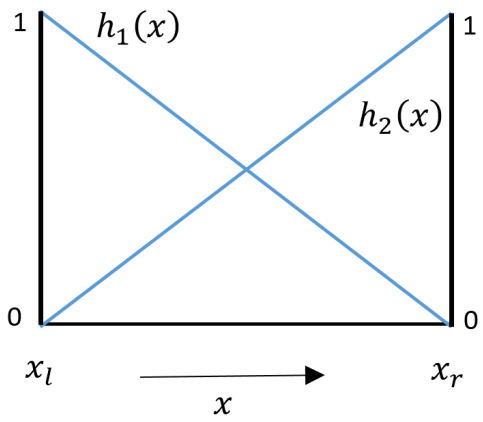

(a) Spatial test functions

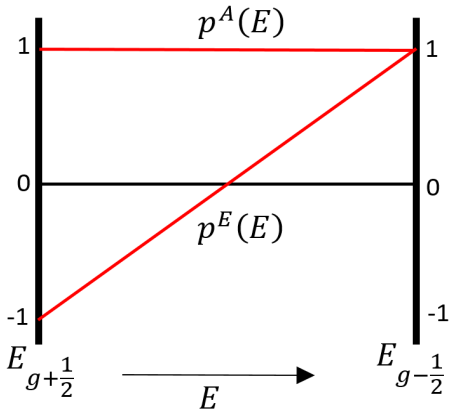

(b) Energy test functions

Figure 3.1: *An illustration of the four test functions. Here x_l and x_r are the left and right x-coordinate of a spatial cell respectively. $E_{g-\frac{1}{2}}$ is the upper boundary and $E_{g+\frac{1}{2}}$ is the lower boundary of an energy group.*

Combining the two previous sections, we can rewrite $\varphi(x,E)$ as a linear combination of both spatial and energy basis functions on element k and group g as

$$\varphi_{k,g}(x,E) = \varphi^A_{k,g}(x)\,p^A + \varphi^E_{k,g}(x)\,p^E_g(E) \tag{3.7}$$

With

$$\varphi^i_k(x) = c^i_{1,k,g}\,h_{1,k}(x) + c^i_{2,k,g}\,h_{2,k}(x) \text{ for } i = A,E \tag{3.8}$$

With $c^i_{1,k,g}$ and $c^i_{2,k,g}$ the coefficients as described in section 3.1.1, so the coefficients for the average and slope part. A visualization of this method is illustrated in figure 3.2

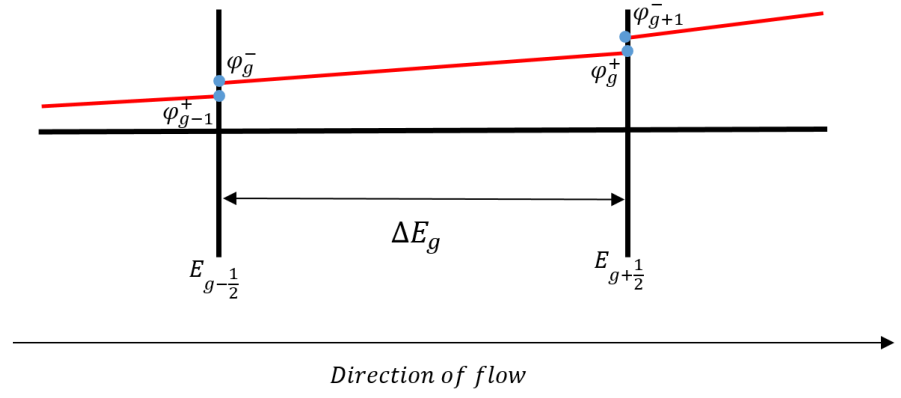

(a) Energy discretization

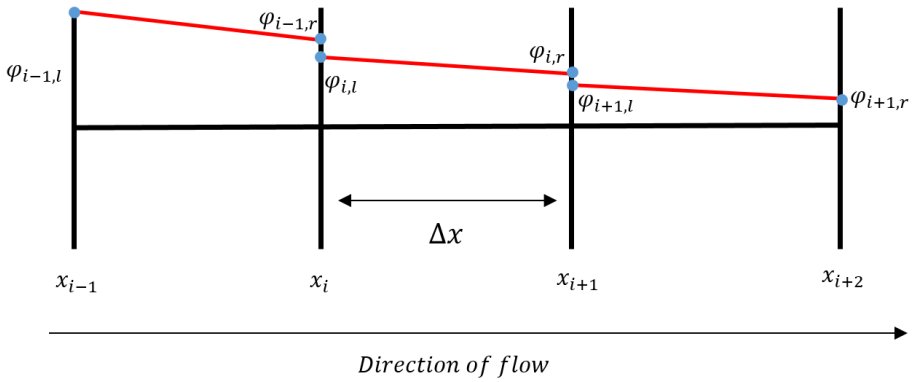

(b) Spatial discretization

Figure 3.2: *An illustration of how the Galerkin method discretizes the flux in both the energy domain (top) and spatial domain (bottom)*

3.2.3. Linear versus constant slope in space

If we want to determine the dose distribution of a proton beam using equations 3.7 and 3.8, we need to solve for 4 coefficients per energy group and spatial element. In realistic cases where we take 3 spatial dimensions and also angular and time dependence into account, a total of about $5{\cdot}10^8$ equations need to be solved, which takes modern high grade computers roughly a few hours. This time is relatively long to be easily implemented in reality, so any reduction in the amount of equations that need to be solved can significantly improve the applicability of this method.

One such reduction in the amount of equations to solve for, is by defining the slope part of the flux to be constant on every spatial domain. This will also cause a decrease in accuracy, which brings us to the main question in this thesis: **is there a significant loss in accuracy when the slope is defined to be constant on every spatial domain?**. The difference between the two situations is illustrated in figure 3.3. Azmy and

Sartori (2010) also mention that this method could significantly decrease the amount of variables to be solved for, but do not further elaborate on the loss of accuracy.

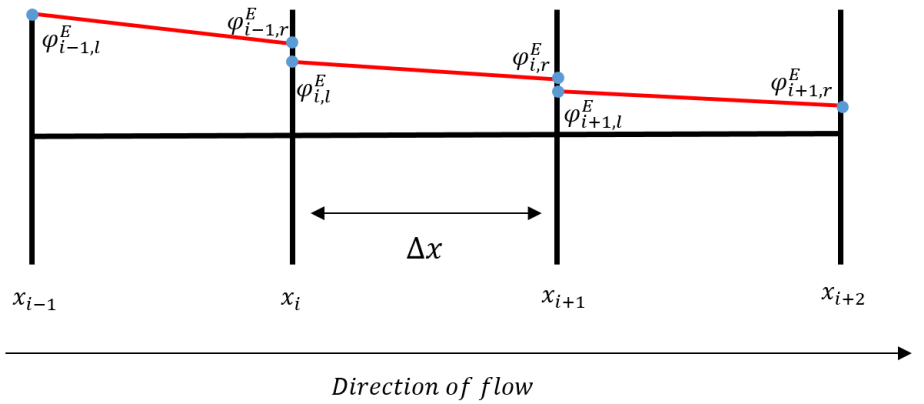

(a) Linear slope

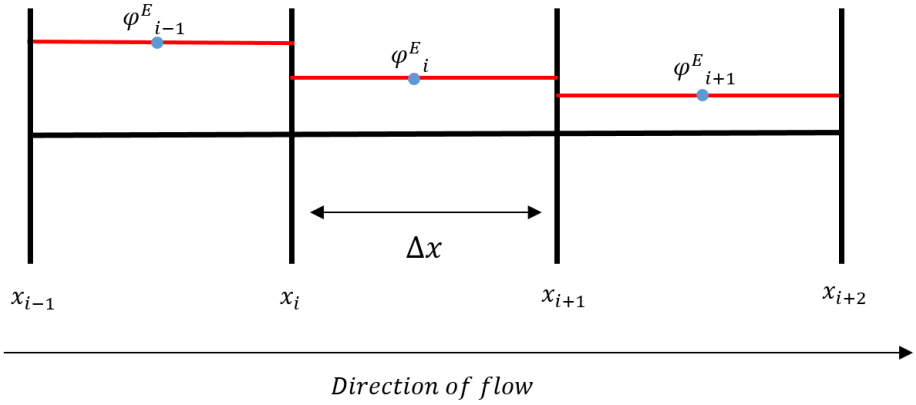

(b) Constant slope

Figure 3.3: *An illustration of the two different methods of describing the slope: linear (top) and constant (bottom)*

3.3. Energy discretization of transport equation terms

In this section we will apply the spatial and energy discretizations described in the previous sections combined with the discontinuous Galerkin method to the terms of equation 2.3 to determine the coefficients of $\boldsymbol{A}$ in 3.1.

3.3.1. Total removal

We start with the total removal term. As mentioned in section 2.1, the total removal term describes the total loss of protons due to any kind of interaction and is defined as

$$\sigma_t \varphi(x, E) \tag{3.9}$$

We choose to have a homogeneous material where $\boldsymbol{\sigma_t = 2}$ **everywhere**. Because this is a straight forward first order term, we will use it in our test cases by adding it to another term of the transport equation, since the resulting equations will have simple analytically solvable solutions. Using these analytical solutions, we can check whether our numerical solutions correctly convergence. First we apply the energy discretization by first multiplying by one of the two energy test functions, writing out $\varphi(x, E)$ as 3.7 and integrating over an

energy group to end up with

$$\int_g \sigma_t \varphi(x,E) p^i(E) dE = \begin{cases} \sigma_t \varphi^A(x) \Delta E_g & \text{for } i = A \\ \frac{1}{3}\sigma_t \varphi^E(x) \Delta E_g & \text{for } i = E \end{cases} \tag{3.10}$$

Because we use two test functions for energy, 3.9 is split up into two separate terms, one for the equations that describe the average value of the flux and one for the slope of the flux. Here we make use of the orthogonality principle, which reduces 3.7 to a single term after multiplication with one of the test functions and integrating.

3.3.2. Streaming

The streaming term describes the streaming of the protons as they travel through a medium and is mathematically defined in one spatial dimension as

$$\frac{\partial \varphi(x,E)}{\partial x} \tag{3.11}$$

The energy discretization of this term is very similar to the total removal term. 3.11 is multiplied by either 3.4 or 3.5 and integrated over a single energy group.

$$\int_g \mu \frac{\partial \varphi(x,E)}{\partial x} p^i(E) dE = \begin{cases} \frac{d\varphi^A(x)}{dx} \Delta E_g & \text{for } i = A \\ \frac{1}{3}\frac{d\varphi^E(x)}{dx} \Delta E_g & \text{for } i = E \end{cases} \tag{3.12}$$

Again the orthogonality of the cross multiplication terms cause the remaining expressions to only be a plain derivative with respect to space instead of a partial one. The application of the Galerkin method has caused the energy dependence to disappear.

3.3.3. CSD

Lastly we will look at the CSD term. The energy discretization is more complicated here because the stopping power is a function of energy too. Multiplying with one of the test functions and integrating gives

$$\int_g \frac{\partial S(E)\varphi(x,E)}{\partial E} p^i(E) dE = -\int_g S(E)\varphi(x,E) \frac{dp^i(E)}{dE} + p^i S(E)\varphi(x,E)\Big|_{E_{g+\frac{1}{2}}}^{E_{g+\frac{1}{2}}} \tag{3.13}$$

With $i = A, E$ again. The first term on the RHS has no contribution for the average part, since the derivative of 3.4 is zero, but it does contribute to the slope part. Because we will eventually solve the system of equations numerically, we will rewrite the stopping power as a linear combination of the values on the energy group boundaries, since this is the only information we will need to determine the coefficients of $\boldsymbol{A}$ in 3.1

$$S(E) = \frac{S_{g+1/2} + S_{g-1/2}}{2} p^A(E) + \frac{S_{g-1/2} - S_{g+1/2}}{2} p^E(E) \tag{3.14}$$

With $S_{g-1/2}$ the stopping power on the upper boundary of energy group g and $S_{g+1/2}$ the stopping power on the lower boundary of energy group g. Writing out the first term on the RHS for $i = E$, with 3.14 and 3.5 gives

$$\int_g S(E)\varphi(x,E) \frac{dp^E(E)}{dE} = \left((S_{g+\frac{1}{2}} + S_{g-\frac{1}{2}})\varphi^A(x) + \frac{1}{3}(S_{g-\frac{1}{2}} - S_{g+\frac{1}{2}})\varphi^E(x) \right) \tag{3.15}$$

To rewrite the second term on the RHS of equation 3.13 we will use the up-winding scheme. This means that we assume that the particles can only flow in a single direction. When the protons flow to the right, the starting point for the calculation of the flux on the left side of cell $k+1$ will be the flux on the right side of cell k. This also means that we only need one boundary condition, since the flux on every cell can be calculated with this condition. We also assume that the stopping power is positive everywhere, since the protons lose energy at every collision. Combining these assumptions, for $g > 1$ the first term can be rewritten into

$$p^i S(E)\varphi(x,E)\Big|_{E_{g+\frac{1}{2}}}^{E_{g+\frac{1}{2}}} = \begin{cases} S_{g-\frac{1}{2}}\left(\varphi^A_{g-1}(x) - \varphi^E_{g-1}(x)\right) + S_{g+\frac{1}{2}}\left(\varphi^A_g(x) - \varphi^E_g(x)\right) & \text{for } i = A \\ S_{g-\frac{1}{2}}\left(\varphi^A_{g-1}(x) - \varphi^E_{g-1}(x)\right) - S_{g+\frac{1}{2}}\left(\varphi^A_g(x) - \varphi^E_g(x)\right) & \text{for } i = E \end{cases} \tag{3.16}$$

Where $\varphi^A_{g-1}(x)$ and $\varphi^E_{g-1}(x)$ are the flux values of the previous group for the average and slope part respectively. If $g = 1$ we will need to define a boundary condition, which must be positive if there are protons streaming into the energy domain from higher energies than the chosen domain or zero for no in-stream of protons from higher energies. We will use both cases in chapter 4. Combining and rewriting the results of the previous sections, we end up with a set of two equations

$$\boxed{\sigma_t \varphi^A_g(x) + \frac{d\varphi^A_g(x)}{dx} + \frac{S_{g+1/2}\big(\varphi^A_g(x) - \varphi^E_g(x)\big)}{\Delta E_g} = \frac{S_{g-1/2}\big(\varphi^A_{g-1}(x) - \varphi^E_{g-1}(x)\big)}{\Delta E_g}} \tag{3.17}$$

$$\boxed{\begin{aligned}\sigma_t \varphi^E_g(x) + \frac{d\varphi^E_g(x)}{dx} + \frac{3\big(S_{g+1/2} + S_{g-1/2}\big)\varphi^A_g(x)}{\Delta E_g} + \frac{\big(S_{g-1/2} - S_{g+1/2}\big)\varphi^E_g(x)}{\Delta E_g} \\ - \frac{3S_{g+1/2}\big(\varphi^A_g(x) - \varphi^E_g(x)\big)}{\Delta E_g} = \frac{3S_{g-1/2}\big(\varphi^A_{g-1}(x) - \varphi^E_{g-1}(x)\big)}{\Delta E_g}\end{aligned}} \tag{3.18}$$

3.4. Spatial discretization of transport equation terms

Now we will apply the chosen spatial discretizations and the Galerkin method to end up with the set of 4 equations we will ultimately solve.

3.4.1. Total removal and CSD

Since σ_t and $S(E)$ are both not functions of space, the spatial discretization is very similar in both cases. We will only write out the method for the first term on the LHS of 3.17 as an example. We multiply with one of the two spatial test functions and integrate over a single spatial element k, which causes the term to split up as follows

$$\begin{aligned}\int_k \sigma_t \varphi^A_k(x) h_{i,k}(x)\,dx &= \int_k \sigma_t \big(a^A_{1,k} h_{1,k}(x) + a^A_{2,k} h_{2,k}(x)\big) h_{i,k}(x)\,dx \\ &= \sigma_t \Big(a^A_{1,k} \int_{x_l}^{x_r} h_{i,k}(x) h_{1,k}(x)\,dx + a^A_{2,k} \int_{x_l}^{x_r} h_{i,k}(x) h_{2,k}(x)\,dx\Big) \text{ for } i = 1,2\end{aligned} \tag{3.19}$$

With x_l and x_r the left and right boundary of spatial cell k respectively. The other terms that contain either σ_t or $S(E)$ have similar outcome and are not written out separately here. Note that the spatial test functions are not orthogonal, so a definite integral remains, which is easily (analytically) solvable.

3.4.2. Streaming

The streaming term needs some more attention since it contains a spatial derivative. Because we don't want to integrate over the derivative of φ, we rewrite this term using the chain rule to get

$$\int_k \frac{d\varphi^j_k(x)}{dx} h_{i,k}(x)\,dx = \int_k \frac{d\varphi^j_k(x) h_{i,k}(x)}{dx}\,dx - \int_k \frac{dh_{i,k}(x)}{dx} \varphi^j_k(x)\,dx \text{ for } i = 1,2$$

With j either A or E. The first term on the RHS can be rewritten as the product of the flux and the test function on the lower and upper integral boundary. This means that the flux on the boundary of each spatial element needs to be defined. We use the up-winding scheme to numerically interpret these boundary values. The principles of the up-winding scheme are mentioned in section 3.3.3. An important consequence of using the up-winding scheme again is that we also need a single boundary condition for space.

To define what the values of the flux actually are on the boundaries, we need to look at two separate cases. When we are not on the outer left boundary of the spatial domain, we simply define that the flux on the left boundary has the same starting point as the flux on the right boundary of the previous element. When we define the flux on the outer left boundary however, we need to choose a function that describes an incoming flux. This so called *boundary flux* can be any function we want, like a mono-energetic δ-peak or a boundary flux for multiple energy groups, also referred to as an *energy plateau*.

The second term on the RHS can be seen as the volumetric streaming term and describes the streaming within each cell. To calculate this integral, rewrite the flux as in 3.8, so the constant term can be taken out of the integral and an integral over just the test functions remains, as in the previous section.

This process of energy and space discretization is repeated until every term is rewritten. The resulting coupled set of four equations is rewritten as a matrix system in the form of 3.1 with $\boldsymbol{A}$ a 4×4 matrix, $\boldsymbol{x}$ a 4×1 vector containing the coefficients a_1 to a_4 and $\boldsymbol{b}$, a 4×1 vector containing all constant terms. We use LU decomposition to solve this system, since this is a fast and accurate way of solving matrix systems which contain only non-zero elements for these kind of numerical problems (Press et al., 1992). The numerical solving is done by using a LAPACK routine (Anderson et al., 1999).

3.5. Choice of stopping power

The stopping power is the rate at which a single proton loses kinetic energy (Paganetti et al., 2011) and it is defined as the negative derivative of energy with respect to space. It differs per material and can be calculated analytically. Bethe (1930) found an analytical formula that accurately describes the stopping power, yet we will make an approximation because we are rather interested in the mathematical outcome rather than the physical outcome of the flux. For this approximation we use the PSTAR database (Berger et al., 2005) to create a relatively accurate analytical expression which we will use in our code.

$$S(E) = \begin{cases} \frac{2\alpha}{\beta E+2} & \text{for E} \geq 8 \cdot 10^4 eV \\ \gamma E^2 \frac{2\alpha}{\beta E+2} & \text{for E} < 8 \cdot 10^4 eV \end{cases} \tag{3.20}$$

With $\alpha = 9.4253 \cdot 10^8$, $\beta = 3.5269 \cdot 10^{-6}$ and $\gamma = 1.5625 \cdot 10^{-10}$. The equation is split into two parts to both follow the PSTAR approximation for most energies, but also go to 0 when E goes to 0. To compare this approximation with the PSTAR approximation, both are plotted in figure 3.4. If we use 0 as lower energy boundary however,

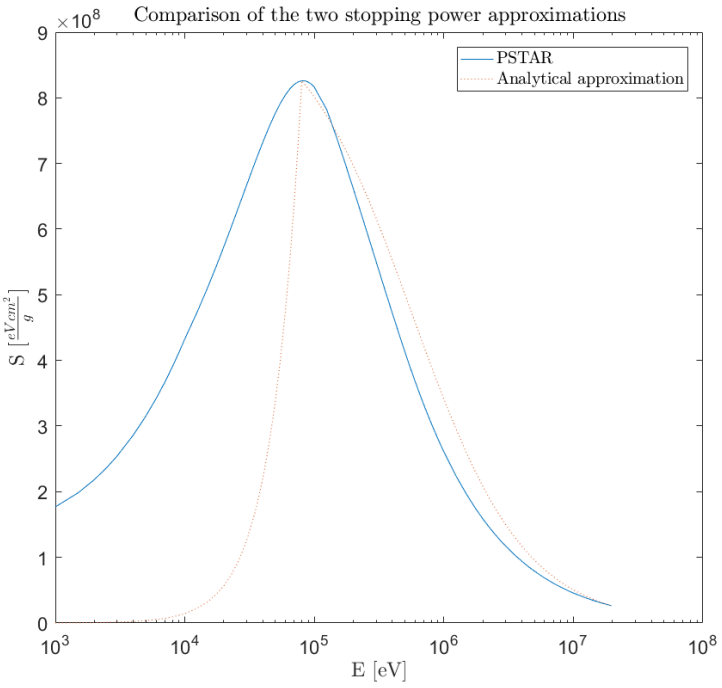

Figure 3.4: *The stopping power of 3.20 compared to the stopping power approximation of PSTAR for water*

errors will be able to occur in the last energy group. If there are traveling particles left in this last energy group while the stopping power is reduced to zero, they will get 'stuck' in this energy range, which could cause a sudden increase in the particle flux. Since we are investigating an effect that is more mathematically relevant than physically, we use $\boldsymbol{2 \cdot 10^6\ eV < E < 1 \cdot 10^8\ eV}$ as our energy range, which is also a typical energy range for protons, so only the part that is inversely proportional to E is used in our code.

3.6. Test cases

To check whether our code and methods work correctly, we will look at two smaller test cases to check if the numerical solutions converge to the analytical ones.

3.6.1. No CSD

Our first case only takes total removal and streaming into account, thus we can use 2.3 without the CSD term. Since we have no energy dependence anymore, we can say $\varphi(x,E) = \varphi(x)$ in this case, to get the following equation

$$\sigma_t \varphi(x) + \frac{d\varphi(x)}{dx} = 0 \tag{3.21}$$

The solution to this equation is a simple exponential function, $\varphi_0 e^{-\sigma_t x}$, with $\sigma_t = 2$ everywhere. The value of φ_0 depends on the boundary condition we use. In chapter 4 we will define this boundary condition and the convergence of the numerical solution to this solution.

3.6.2. No streaming

The second case is one where only total removal and CSD are present. Rewriting 2.3 without streaming gives

$$\sigma_t \varphi(E) - \frac{\partial S(E)\varphi(E)}{\partial E} = 0 \tag{3.22}$$

Since this is a test case, we will use a constant value for $S(E)$, e.g. $5 \cdot 10^7$ everywhere on the domain (so $S(E) = S \neq f(E)$), instead of using 3.20. The solution is again a simple exponential function:

$$\varphi(E) = \frac{\varphi_{E_{max}}}{e^{\frac{\sigma_t}{S} E_{max}}} e^{\frac{\sigma_t}{S} E} \tag{3.23}$$

With $\varphi_{E_{max}}$ the value of the flux at the upper energy boundary E_{max}, so the in-stream of particles with higher energies, which can be chosen to be either a positive number or zero. In chapter 4 we will check the convergence of the numerical solution to this one.

4

Results and conclusions

4.1. Test cases

To get to equations 3.17 and 3.18 we needed to make a few approximations to simplify some numerically hard to solve expressions. To check if the resulting numerical solutions converge to the reference solutions and for what level of discretization, we analyze the error between them as function of discretization level in this section. The RMS error ϵ is calculated in the following way:

$$\epsilon = \frac{\sqrt{\iint \left(\varphi_{ref}(x,E) - \varphi_{num}(x,E)\right)^2 dxdE}}{\sqrt{\iint \left(\varphi_{ref}(x,E)\right)^2 dxdE}} \tag{4.1}$$

Where φ_{ref} and φ_{num} are the reference and numerical solution respectively. For the test cases, we use an analytical solution as reference solution and the double integrals become single integral, since φ only depends on either space or energy in the test cases. When we solve 2.3 in total, we will use another reference solution, which will also be numerically generated, but with a high level of both spatial elements and energy groups to create an accurate approximation of the smooth solution. The integrals stated in 4.1 are solved numerically, which is done by using the Gaussian quadratures. This is based on the mathematical principle that an integral can be approximated by a sum of weighted function evaluations (Press et al., 1992).

4.1.1. No CSD

In our first test case, we numerically solve 3.21 and see if it convergence to an analytically determined reference solution. This equation has a simple exponential function as solution and this is plotted together with the numerical solution for 10 spatial elements of equal width. As boundary condition, we define φ_0 to be 1 $cm^{-2}s^{-1}$on $x = 0$.

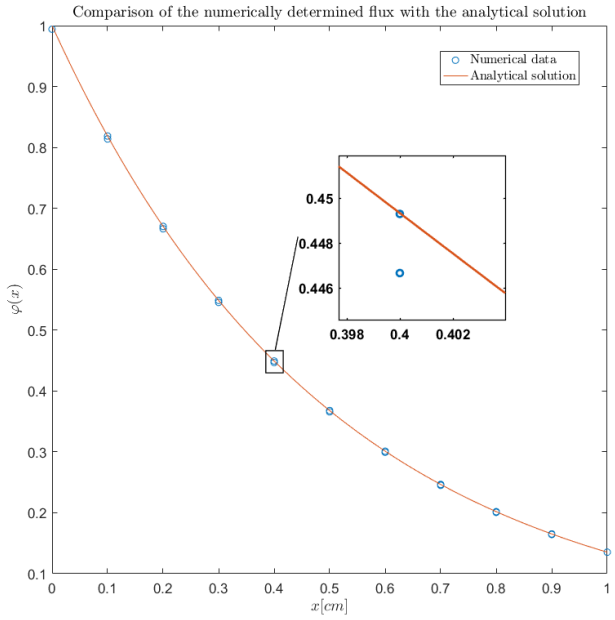

Figure 4.1: *Numerical outcome compared to the analytical solution, e^{-2x}, of equation 3.21 for 10 spatial elements. On the zoomed in subplot we see the discontinuity on an element boundary*

In figure 4.1, the data points lie almost exactly on the line of the exponential function. On the boundary of each spatial element are two data points, because we use a discontinuous method for solving the equations. As Δx becomes smaller, the discontinuous approximation should converge to the analytical continuous solution. To verify this, the error ϵ as function of Δx is plotted in figure 4.2.

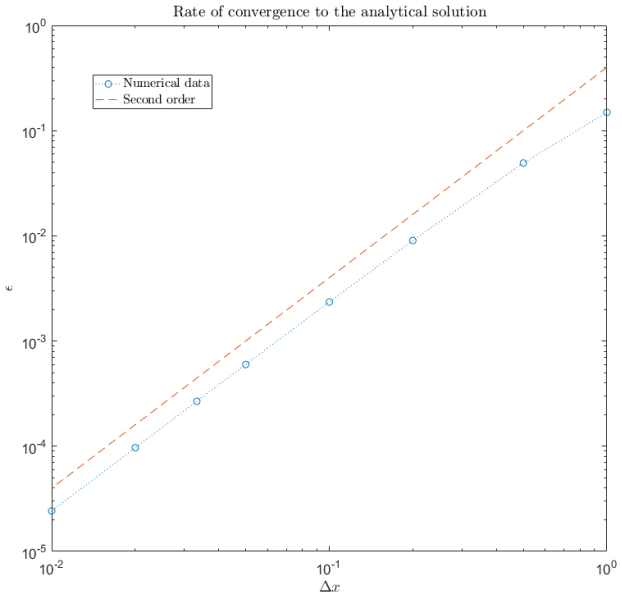

Figure 4.2: *The error ϵ, computed with equation 4.1, as function of Δx on a log-log scale. For one or two elements, the numerical solution does not strongly convergence to the analytical one, but as the number of spatial elements increases, the numerical data convergences quadratically*

As Δx becomes smaller, the error becomes smaller too with a slope on a log-log scale that converges to 2

for fine spatial grids, so we can say that for a sufficient number of elements $\epsilon \propto (\Delta x)^2$. From figures 4.1 and 4.2 we can conclude that our code solves the streaming part correctly, so we can continue with analyzing whether this also holds for the stopping power term, from where we can add all three terms to come to a correct numerical solution for 2.3.

4.1.2. No streaming

Now we will look at our second test case, where only CSD and total removal are present. We let our code solve 3.22, with the boundary condition that the instream from particles of energies higher than $1 \cdot 10^8$ is 1 $cm^{-2}s^{-1}$ and the boundary flux on $x = 0$ is 1 everywhere. The value we use for our stopping power and the analytical solution are mentioned in 3.6.2. The numerical data points are compared to the analytical solution in figure 4.3

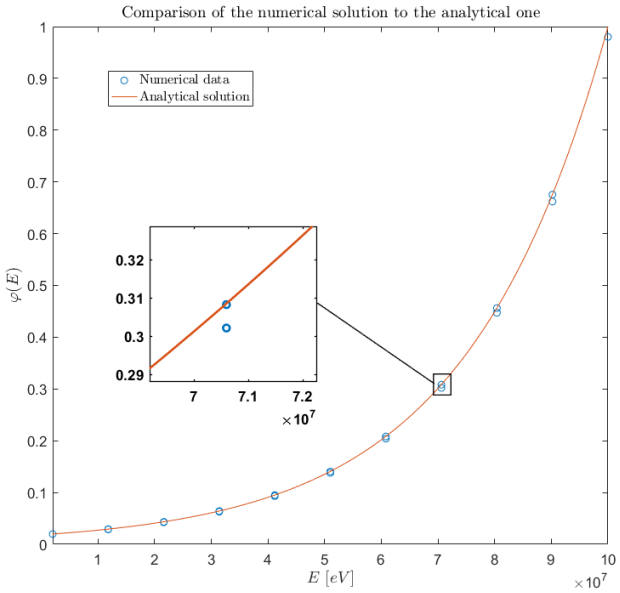

Figure 4.3: *Numerically computed data points compared to the analytical solution of equation 3.22 for 10 energy groups. In the subplot, a zoomed in image is displayed, where the discontinuity on a group boundary is visible.*

The numerical result is very close to the analytical result for just 10 energy groups. As the number of groups increases, ΔE decreases and so should the error. To analyze at what rate this occurs, we have plotted the error as a function of ΔE on a log-log scale.

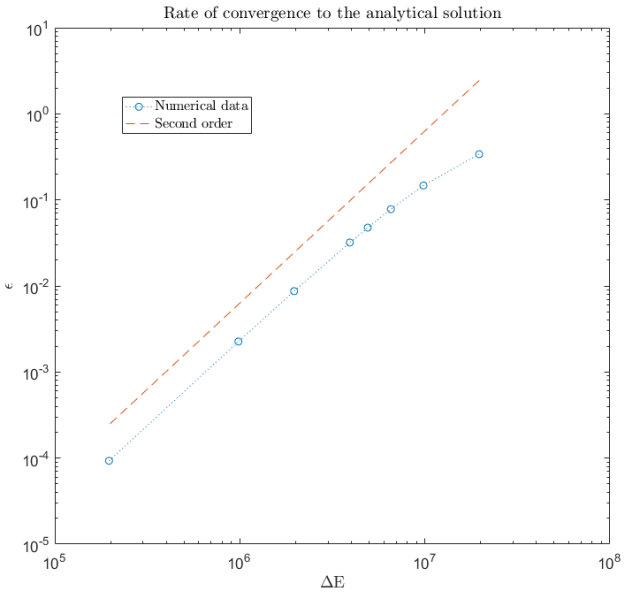

Figure 4.4: *The error ϵ as a function of ΔE on a log-log scale. The order of convergence seems to be quadratic for sufficiently fine grids.*

Again the slope of the line in figure 4.4 converges to 2 for fine energy grids, which means that we could conclude that $\epsilon \propto (\Delta E)^2$ for $\lim_{\Delta E \to 0}$. Now we have made sure that the numerical approximation of both the stopping power and the streaming is correct. The last step is to solve the equation 2.3 in total for two different cases: one where the slope is linear on each spatial element and one where the slope is constant, while changing the number of either spatial elements or energy groups. For both cases we will also use two separate boundary conditions to determine their effect. The boundary conditions are set at $x = 0$ and are either a δ-peak or an energy plateau. The main mathematical difference between these two is that the energy plateau will be defined as a smooth function everywhere, while the δ-peak will be discontinuous, which will most likely cause numerical errors. The in-stream of particles of higher energies is set to 0.

4.2. Convergence in E for the total equation

For tables of the data used in the coming sections, the reader is referred to the appendices.

First we will look at how ϵ converges as function ΔE and what φ looks like as function of energy on a certain spatial cell. We have defined the δ-peak as a boundary flux that has the value $\frac{1}{\Delta E}$ for a specific energy group and 0 for other groups.

4.2.1. δ-peak as boundary condition

Let us start with a δ-peak on the boundary. In figure 4.7, the flux is plotted as function of energy for the total energy domain we consider in our code. We have used 128 spatial groups to generate this result and we set x to be the left boundary of the middle element.

The effect of the discontinuous boundary condition is clearly visible, as the numerical solution with the widest energy groups struggles to reach the height of the reference solution. As the number of groups increases, the width of the homogeneous energy groups decreases and the solution converges to the reference solution in both cases, though there are differences. For the case with a linear slope in space, the numerical solution with 1024 groups seems to reach the reference solution more closely at the top than for the case where we have a constant slope in space. We could think that this also means that the slope of ϵ as function of ΔE will converge to a higher value for the linear slope. If we look closely however, we see that at the negative bumps next to the top the opposite happens: the numerical solution of the right figure follows the reference solution more accurately. This could be caused by the discontinuity of the δ-peak, which expresses itself in different ways for the two cases. To qualitatively know the order of convergence we calculate the error with 4.1. The resulting ϵ is plotted as function of ΔE for both cases in figure 4.6

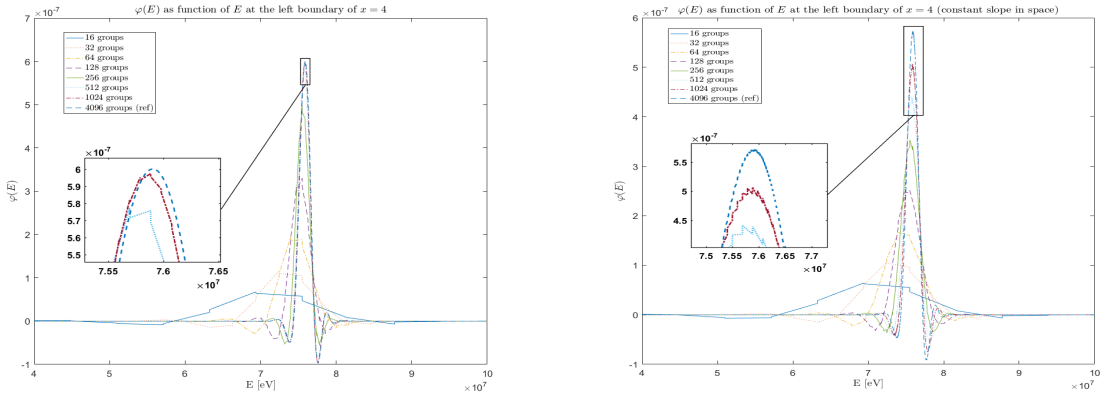

(a) Linear slope in space

(b) Constant slope in space

Figure 4.5: *A plot of $\varphi(E)$ for different amounts of energy groups on a partial energy domain for both a linear slope in space (left) and a constant slope in space (right). It seems that for a linear slope in space, the numerical solution converges to the reference solution at the top of the peak at a faster rate than for a constant slope, while the bumps on either side are less accurately followed.*

Unlike what we concluded from the test cases, for both a linear and constant slope the order of the error seems to converge to 1 instead of 2. The left figure seems to have data points that converge slightly stronger than the right figure, but the difference is not big. To see if the main cause of this loss in rate of convergence is caused by the discontinuous δ-peak, in the next section we will display the above cases with a continuous energy plateau as boundary condition.

4.2.2. Energy plateau as boundary condition

For our energy plateau we use a continuous function, which reaches zero at our energy domain boundaries and is nonzero in between. It is defined as

$$\phi_{plateau} = \frac{1}{2}\left(\cos\left(\left(2\frac{E}{E_{max}} - 1\right)\pi\right) + 1\right) \tag{4.2}$$

First we will look at how this boundary condition affects $\varphi(E)$ at a certain depth. We use the same amount of spatial elements and depth as in the previous subsection.

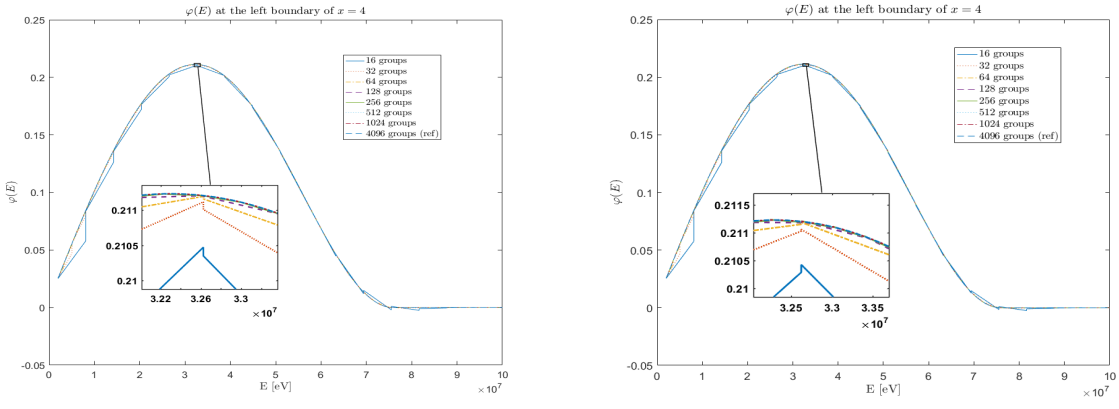

(a) Linear slope in space

(b) Constant slope in space

Figure 4.7: *A plot of $\varphi(E)$ for different amounts of energy groups on a partial energy domain for both a linear slope in space (left) and a constant slope in space (right). As boundary condition we used a smooth energy plateau, defined by 4.2. In both cases only the coarse solutions are distinguishable from the other ones, until we reach around 128 groups, where the difference in the solution becomes to small to be visible in these figures.*

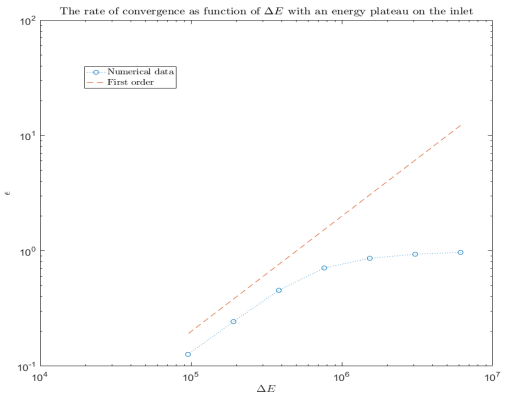

(a) Linear slope in space

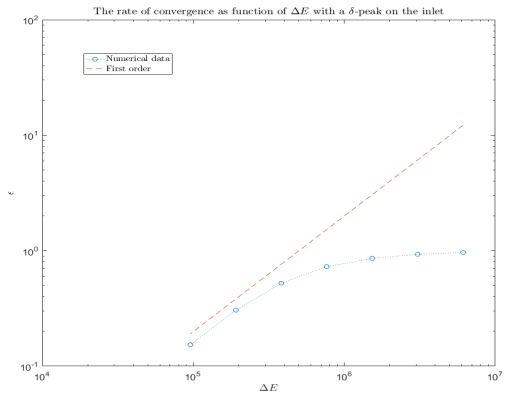

(b) Constant slope in space

Figure 4.6: *A log-log plot of ϵ as function of ΔE for both a linear slope in space (left) and a constant slope in space (right). Both seem to convergence to a slope of* 1 *on a logarithmic scale at about the same rate.*

The form that this plot has is what we would expect, because we are looking at cross-section somewhere in the middle. At this point, high energetic protons have lost some of their energy due to collisions, causing the absence of high energetic particles in the plots.

For both cases the plots of $\varphi(E)$ for different energy group width seems to be practically the same. The mirrored effect that the zoomed in subplots seem to have is caused by small differences of the boundary values of the neighboring energy groups and will probably not affect the determination of the RMS error. From about 128 energy groups, the difference between the numerical solutions and the reference solution is not visible anymore in these plots, but they also do not contain much useful information for our research, as we are interested in the order of convergence. Since we do not have to deal with the effect that the numerical solution has to 'grow' to the reference solution as with the δ-peak, the slope of the error will probably converge to a value higher than 1. To check whether this is true, we determined the quantitative RMS error and plotted it on a log-log scale in figure 4.8

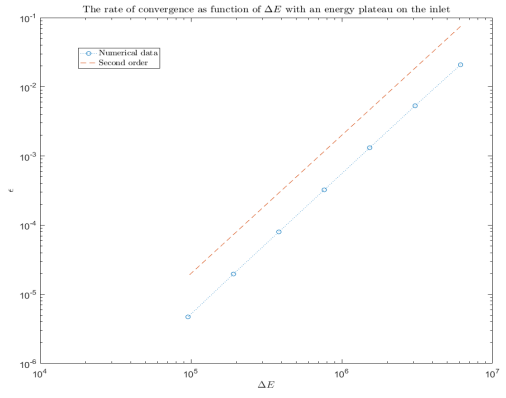

(a) Linear slope in space

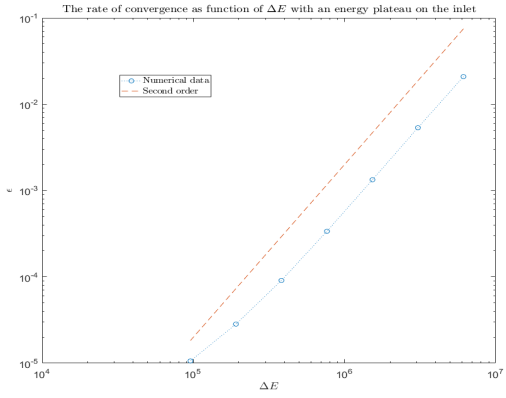

(b) Constant slope in space

Figure 4.8: *A log-log plot of ϵ as function of ΔE for both a linear slope in space (left) and a constant slope in space (right) with a smooth energy plateau as boundary condition. Both seem to convergence to a slope of* 2 *on a logarithmic scale, but the case with constant slope loses accuracy as the number of groups increases.*

In these figures the effect of the method of discretization is more clearly visible. For the first few coarse numerical solutions, the error decreases quadratically as the width of the energy groups decreases. When we use 128 or more energy groups however, we start to see a decrease in this quadratic order for the constant

slope case. At the finest numerical solution, that has 1024 groups, the order of the error has decreased to 1.4175, while the slope of ϵ for the linear case remains a bit above 2 on a logarithmic scale.

4.3. Convergence in x for the total equation

Secondly we will look at the convergence of ϵ as function of Δx. We will use the same boundary conditions as in the previous section. Since $\varphi(x)$ does not contain much useful information for our research, they will not be displayed. We set the amount of reference groups to 128 in all cases.

4.3.1. δ-peak as boundary condition

We will start with displaying the plots of the error as function of the spatial cell width.

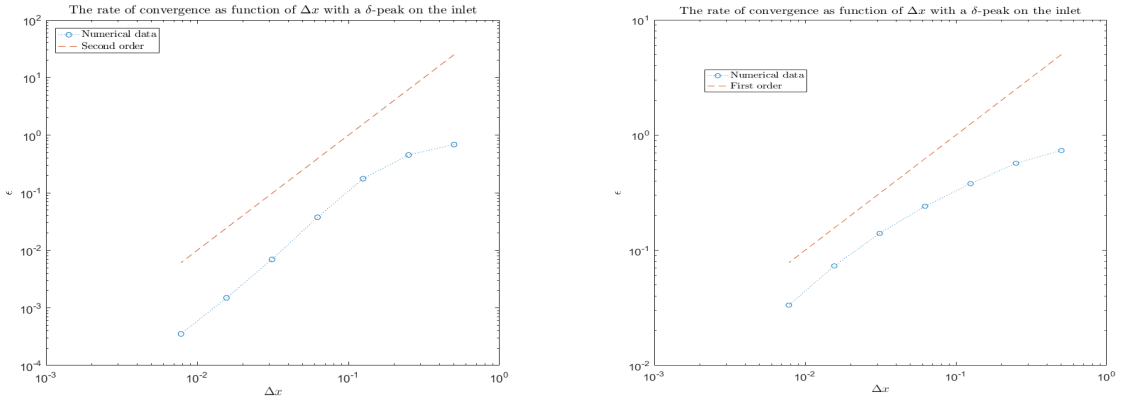

(a) Linear slope in space

(b) Constant slope in space

Figure 4.9: *A log-log plot of ϵ as function of Δx for both a linear slope in space (left) and a constant slope in space (right) with a δ-peak as boundary condition. The convergence of both cases is quite different, as the left figure seems to converge to a quadratic order while the right figure does not seem to converge at all.*

For the linear case, the slope of the error on a logarithmic scale rapidly increases and exceeds 2, where after it decreases again and seems to converge back to 2. This is a similar result we had in our first test case. For the constant slope in space however, the slope does not converge at all. The order also increases at a non-constant rate, so it is not possible to conclude anything about the rate of convergence of the constant slope case in this situation, aside from the fact that it converges significantly slower than the linear case for our generated data.

4.3.2. Energy plateau as boundary condition

Lastly we will look at the course of the error as function of Δx with the smooth energy plateau defined by 4.2 as boundary condition. In figure 4.10, we compare the constant case to the linear case.

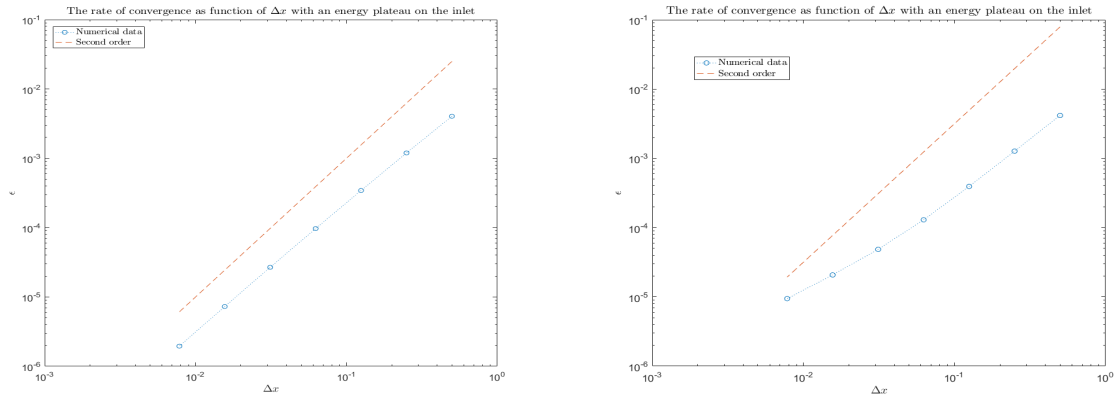

(a) Linear slope in space

(b) Constant slope in space

Figure 4.10: *A log-log plot of ϵ as function of Δx for both a linear slope in space (left) and a constant slope in space (right) with an energy plateau boundary condition. The convergence of both cases is quite different, as the left figure seems to converge to a quadratic order while the right figure does not seem to converge at all again.*

Comparing figures 4.9 and 4.10, it is clearly visible that the boundary condition also influences the convergence of Δx. The bump that occured in figure 4.9 (a) is not present in figure 4.10 (a), although they both converge to a quadratic order. The constant case again does not seem to converge to any number, but with the energy plateau as boundary condition, it seems to start at a higher order and decrease, instead of increase from a lower value. The tables in appendix A show that both cases reach a value of around 1.13 in the end, but from this data it is not clear what the exact value could be.

4.4. Error in integral value

So far we have calculated the relative errors by using taking the RMS of the angular flux. As mentioned in the first chapter, the most practical information is generated by determining the dose, which is defined by

$$D = \int_{space} \frac{E_{deposited}(x)}{\rho(x)} \tag{4.3}$$

With D the delivered dose, $E_{deposited}$ the amount of energy deposited in the material and ρ the density of the material. Since the deposited energy can be determined by integrating the flux over the whole used energy domain, we are also interested in a different kind of error measurement. This second method of error calculation is defined as

$$\eta = \frac{\left|\iint \varphi_{num}(x,E) - \varphi_{ref}(x,E)dxdE\right|}{\iint \varphi_{ref}dxdE} \tag{4.4}$$

The numeric values of the errors and the slope are stated in appendix B. We use 128 elements again for the cell quantity that is held constant. From these tables we can conclude that for a δ-peak as boundary condition, η converges randomly, as none of the orders seem to converge to a certain value as the number of spatial cells or energy groups increases. The interesting information is displayed in the lower tables, where we have an energy plateau on the boundary. The order of convergence remains to be 2 for both spatial discretizations and the loss in order for higher amounts of energy groups does not occur for the constant slope case. A remarkable result is found when we have an energy plateau on the boundary and look at convergence as function of Δx. For a linear slope in space, an order is 'won', as the convergence seems to go with a slope of 3 on a logarithmic scale. The implications and reason behind this gain in order will need further research to determine the cause. For a constant slope in space, the order seems to decrease at a non-uniform rate and it is unclear if and to what value the slope converges to. The same effect is visible when we plotted ϵ versus Δx in the same case.

4.5. Main conclusions

There are significant differences between the test cases and the total cases in terms of order of convergence. The use of a discontinuous boundary condition seems to cause a loss in this order for the convergence of ϵ as function of ΔE and there is not much different if either a linear or constant slope is used. A continuous boundary condition however seems to retain the quadratic convergence in both cases.

For the convergence of ϵ as function of Δx, the choice of either a linear or constant slope for the spatial discretization has a bigger effect. When we use the δ-peak as boundary condition and a constant slope in space, there seems to be no convergence of the order of the error, but it tends to have a lower order than 2. For a linear slope in space the order of 2 is contained. This means that for a discontinuous boundary condition, the case with the linear slope in space has less trouble to converge to the reference solution. For a continuous boundary condition, the linear slope again retains its order of convergence, while the constant slope case does not seem to converge to a certain value. The slope starts at around 2 on a logarithmic scale but decreases non-uniformly as the number of spatial cells increases. At 1024 spatial elements, the value of the slope however does converge to a value around 1.13, as does the non-converging error at the δ-peak boundary condition. The effect of the error calculated by η needs further research before any solid conclusions can be drawn.

5

Discussion

The main goal of this research was to investigate what the effect was of using a different kind of spatial discretization for solving the 2-dimensional Boltzmann-Fokker-Planck equation. The main question was: "**is there a significant loss in accuracy when the slope is defined to be constant on every spatial domain?**". In this chapter we will try to answer this question and discuss some of the results we found and their relevance. Lastly, we will mention some ideas for future research that could be done on this subject.

5.1. Elaboration of results

In the end of the previous chapter, we concluded that the choice of either a constant or linear slope in space and the kind of boundary condition strongly influences the order of the convergence of the error. It might not be surprising that the boundary conditions, which are functions of energy, affect the convergence of ΔE and that the choice of spatial discretization has a strong influence on the convergence of Δx. There does seem to be some kind of interaction between the two however. To analyze this effect, we have created some additional results for ϵ as function of Δx where chose other values of amount of reference groups for both spatial discretizations with an energy plateau as boundary condition. Since we are mostly interested in the limit for Δx or ΔE to zero, we have only determined the error of the four most fine numerical cases. The errors are calculated using 4.1. An overview is given in table 5.1

Table 5.1: *The RMS error for different amounts of reference groups and spatial cells, for both spatial discretization cases*

(a) 512 reference groups

Number of spatial elements	ϵ (linear slope)	Order (linear slope)	ϵ (constant slope)	Order (constant slope)
128	$9.73365 \cdot 10^{-5}$	-	$1.01125 \cdot 10^{-4}$	-
256	$2.68779 \cdot 10^{-5}$	1.8566	$2.94255 \cdot 10^{-5}$	1.7829
512	$7.23128 \cdot 10^{-6}$	1.8941	$9.01335 \cdot 10^{-6}$	1.7089
1024	$1.88104 \cdot 10^{-6}$	1.9427	$3.07766 \cdot 10^{-6}$	1.5483

(b) 1024 reference groups

Number of spatial elements	ϵ (linear slope)	Order (linear slope)	ϵ (constant slope)	Order (constant slope)
128	$9.74254 \cdot 10^{-5}$	-	$9.89065 \cdot 10^{-4}$	-
256	$2.69266 \cdot 10^{-5}$	1.8553	$2.78061 \cdot 10^{-5}$	1.8307
512	$7.24051 \cdot 10^{-6}$	1.8949	$7.82310 \cdot 10^{-6}$	1.8296
1024	$1.88142 \cdot 10^{-6}$	1.9443	$2.28121 \cdot 10^{-6}$	1.7779

(c) 2048 reference groups

Number of spatial elements	ϵ (linear slope)	Order (linear slope)	ϵ (constant slope)	Order (constant slope)
128	$9.74460 \cdot 10^{-5}$	-	$9.80601 \cdot 10^{-5}$	-
256	$2.69495 \cdot 10^{-5}$	1.8543	$2.72763 \cdot 10^{-5}$	1.8460
512	$7.25368 \cdot 10^{-6}$	1.8935	$7.45132 \cdot 10^{-6}$	1.8721
1024	$1.88395 \cdot 10^{-6}$	1.9450	$2.01307 \cdot 10^{-6}$	1.8881

(d) 4096 reference groups

Number of spatial elements	ϵ (linear slope)	Order (linear slope)	ϵ (constant slope)	Order (constant slope)
128	$9.74495 \cdot 10^{-5}$	-	$9.77245 \cdot 10^{-4}$	-
256	$2.69547 \cdot 10^{-5}$	1.8541	$2.70885 \cdot 10^{-5}$	1.8510
512	$7.25989 \cdot 10^{-6}$	1.8925	$7.33199 \cdot 10^{-6}$	1.8854
1024	$1.88755 \cdot 10^{-6}$	1.9434	$1.93046 \cdot 10^{-6}$	1.9253

These tables give an interesting result: the order of error remains quadratically for the linear case, while there seems to be a turning point at 2048 reference groups for the constant slope case. When we use less than 2048 reference groups to check the rate of convergence of ϵ as function of Δx, there seems to be a decreasing convergence starting somewhere at 2, but when we use 2048 or more reference groups, the order starts to converge to 2. Surprisingly, we could conclude that the latter case will only converge to 2 for both $\lim_{\Delta x \to 0}$ and $\lim_{\Delta E \to 0}$.

5.2. Significance of results

The results formed in this research are generated by defining a number of quantities, like σ_t, $S(E)$ and the boundary condition. We have used relatively simple expressions for these quantities, while in reality these will be a lot more influenced by the kind of material and energies used, causing them to possibly lack much physical relevance. Their mathemathic relevance is of greater value however, since we have been mostly interested in macroscopic orders, which are likely to remain in a more physical realistic case.

In the 'big' code that will try to solve a more complete problem than described here, which contains angular dependence and space in three dimensions, about 100 spatial elements and about the same order of energy groups will be used. The results described in chapter 4 could therefore be considered as relevant for this complete problem. The tables stated in the previous section however give an indication of some form of coupling between space and energy. The exact implications of this effect needs to be analyzed further until we can make more solid conclusions for the application of these results on the complete case.

5.3. Final conclusions and suggestions for future work

To conclude our research, we will try to answer the question stated in chapter 3: "**is there a significant loss in accuracy when the slope is defined to be constant on every spatial domain?**". Using the results of chapter 4 we could conclude that there is not much loss in accuracy in the order of convergence for the energy domain. A discontinuity in the boundary condition does cause loss of accuracy. In the complete case described in the previous section, an energy plateau is used which is defined as a group of δ-peaks, so in future research the effect of a more realistic boundary condition could be used to determine its effect on the convergence in the energy domain. For our spatial domain, the boundary condition is less relevant, but the choice of spatial discretization is. A constant slope in space seems to cause a loss in order of convergence for 128 reference groups. From section 5.1 a different conclusion follows however. The coupling of space and energy and their effect on the convergence needs to be analyzed further in future research for us to be able to conclude if there will be a loss in accuracy when the constant discretization method is used in the complete case.

Another smaller test case that could be done is the use of an linear stopping power instead of the stopping power we have used, as defined by 3.20. Since we use a linear approximation for our stopping power in our calculations, a linearly defined stopping power could cause a more accurate result than a stopping power that is inversely proportional to energy, though it will be less relevant physically.

A

Tables of error data of section 4.2 and 4.3

A.1. Convergence in x

A.1.1. Linear slope in space

Table A.1: *ϵ for different normalised values of $\frac{\Delta x}{L}$, together with the rate of change on a log-log scale for different boundary conditions. We have used a linear slope in space as spatial discretization and 128 energy groups to generate these results.*

(a) δ-peak on the inlet

$\frac{\Delta x}{L}$	ϵ	Slope on a log-log scale
2^{-4}	$6.8751234393366500 \cdot 10^{-1}$	-
2^{-5}	$4.5282152526693997 \cdot 10^{-1}$	0.6024
2^{-6}	$1.7547039835374201 \cdot 10^{-1}$	1.3677
2^{-7}	$3.7479388080701580 \cdot 10^{-2}$	2.2271
2^{-8}	$6.9565602634032277 \cdot 10^{-3}$	2.4297
2^{-9}	$1.4925389734957121 \cdot 10^{-3}$	2.2206
2^{-10}	$3.5374971767940933 \cdot 10^{-4}$	2.0770

(b) Energy plateau on the inlet

Δx	ϵ	Slope on a log-log scale
2^{-4}	$4.039787386580717 \cdot 10^{-3}$	-
2^{-5}	$1.19470596475327 \cdot 10^{-3}$	1.7576
2^{-6}	$3.435188068881923 \cdot 10^{-4}$	1.7982
2^{-7}	$9.692104115415741 \cdot 10^{-5}$	1.8255
2^{-8}	$2.683707088756518 \cdot 10^{-5}$	1.8526
2^{-9}	$7.284108685679798 \cdot 10^{-6}$	1.8814
2^{-10}	$1.952281313136042 \cdot 10^{-6}$	1.8996

A.1.2. Constant slope in space

Table A.2: *ϵ for different normalised values of $\frac{\Delta x}{L}$, together with the rate of change on a log-log scale for different boundary conditions. We have used a constant slope in space as spatial discretization and 128 energy groups to generate these results*

(a) δ-peak on the inlet

Δx	ϵ	Slope on a log-log scale
2^{-4}	$7.3454242246263102 \cdot 10^{-1}$	-
2^{-5}	$5.6948525983912601 \cdot 10^{-1}$	0.3672
2^{-6}	$3.7892972223605698 \cdot 10^{-1}$	0.5877
2^{-7}	$2.4139469528162300 \cdot 10^{-1}$	0.6505
2^{-8}	$1.4040990776535300 \cdot 10^{-1}$	0.7817
2^{-9}	$7.3216644840841921 \cdot 10^{-2}$	0.9394
2^{-10}	$3.3436957973512441 \cdot 10^{-2}$	1.1307

(b) Energy plateau on the inlet

$\frac{\Delta x}{L}$	ϵ	Slope on a log-log scale
2^{-4}	$4.160554271123949 \cdot 10^{-3}$	-
2^{-5}	$1.270339937141631 \cdot 10^{-3}$	1.7116
2^{-6}	$3.923508699914549 \cdot 10^{-4}$	1.6950
2^{-7}	$1.295420354742993 \cdot 10^{-5}$	1.5987
2^{-8}	$4.854349466188812 \cdot 10^{-5}$	1.4161
2^{-9}	$2.074924812760828 \cdot 10^{-5}$	1.2262
2^{-10}	$9.431942775142822 \cdot 10^{-6}$	1.1374

A.2. Convergence in E

A.2.1. Linear slope in space

Table A.3: *ϵ for different normalised values of ΔE, together with the rate of change on a log-log scale for different boundary conditions. We have used 128 spatial elements and a linear slope in space to generate these results.*

(a) δ-peak on the inlet

$\frac{\Delta E}{E_{max}}$	ϵ	Slope on a log-log scale
2^{-4}	$9.6906367320166498 \cdot 10^{-1}$	-
2^{-5}	$9.3398684866791504 \cdot 10^{-1}$	0.0532
2^{-6}	$8.6132856423376802 \cdot 10^{-1}$	0.1168
2^{-7}	$7.1024157056524995 \cdot 10^{-1}$	0.2783
2^{-8}	$4.5531166015798702 \cdot 10^{-1}$	0.6415
2^{-9}	$2.4342185621452700 \cdot 10^{-1}$	0.9034
2^{-10}	$1.2653987486303600 \cdot 10^{-1}$	0.9439

(b) Energy plateau on the inlet

$\frac{\Delta E}{E_{max}}$	ϵ	Slope on a log-log scale
2^{-4}	$2.085456453760607 \cdot 10^{-2}$	-
2^{-5}	$5.325183854377679 \cdot 10^{-3}$	1.9695
2^{-6}	$1.317548420159612 \cdot 10^{-3}$	2.0150
2^{-7}	$3.243485429999464 \cdot 10^{-4}$	2.0222
2^{-8}	$7.995141783240467 \cdot 10^{-5}$	2.0203
2^{-9}	$1.966101392311136 \cdot 10^{-5}$	2.0238
2^{-10}	$4.715713368666641 \cdot 10^{-6}$	2.0598

A.2.2. Constant slope in space

Table A.4: *ϵ for different normalised values of ΔE, together with the rate of change on a log-log scale for different boundary conditions. We have used 128 spatial elements and a constant slope in space to generate these results.*

(a) δ-peak on the inlet

$\frac{\Delta E}{E_0}$	ϵ	Slope on a log-log scale
2^{-4}	$9.6706989301097901 \cdot 10^{-1}$	-
2^{-5}	$9.3040896756602598 \cdot 10^{-1}$	0.0558
2^{-6}	$8.5859317094827803 \cdot 10^{-1}$	0.1159
2^{-7}	$7.2696491137946595 \cdot 10^{-1}$	0.2401
2^{-8}	$5.2266221403644797 \cdot 10^{-1}$	0.4760
2^{-9}	$3.0525688526311301 \cdot 10^{-1}$	0.7759
2^{-10}	$1.5344851002414200 \cdot 10^{-1}$	0.9923

(b) Energy plateau on the inlet

$\frac{\Delta E}{E_0}$	ϵ	Slope on a log-log scale
2^{-4}	$2.088689936530416 \cdot 10^{-2}$	-
2^{-5}	$5.346552886212842 \cdot 10^{-3}$	1.9659
2^{-6}	$1.333433095933789 \cdot 10^{-3}$	2.0035
2^{-7}	$3.374291872822577 \cdot 10^{-4}$	1.9825
2^{-8}	$9.096070307967407 \cdot 10^{-5}$	1.8913
2^{-9}	$2.834541176825406 \cdot 10^{-5}$	1.6821
2^{-10}	$1.061172080520173 \cdot 10^{-5}$	1.4175

B

Tables of error data of section 4.4

B.1. δ-peak on the inlet

Table B.1: $\log\Delta\eta$ *as function of* ΔE *for different amounts of energy groups with a* δ*-peak on the inlet. The exact values of the double integrals over space and energy are also given. Data is generated using 128 spatial elements.*

(a) Linear slope in space

Number of groups	Integral value	Logarithm of $\Delta\eta$ with respect to E
2^4	6.61880370519984	-
2^5	6.59876582775515	2.2864
2^6	6.59360913049872	9.0361
2^7	6.59359830208165	3.3177
2^8	6.59359938972587	3.2940
2^9	6.59359924658701	1.2432
2^{10}	6.59359916548608	-1.5400
2^{12} (ref)	6.59359928909550	

(b) Constant slope in space

Number of groups	Integral value	Logarithm of $\Delta\eta$ with respect to E
2^4	6.61782829944475	-
2^5	6.60370429866655	1.2617
2^6	6.59237815008147	3.0488
2^7	6.59365146574764	4.5486
2^8	6.59359774637737	5.0812
2^9	6.59359934417701	4.7703
2^{10}	6.59359916435188	-1.1270
2^{12} (ref)	6.59359928769914	

Table B.2: $\log\Delta\eta$ *as function of* Δx *for different amounts of spatial cells with a* δ*-peak on the inlet. The exact values of the double integrals over space and energy are also given. Data is generated using 128 energy groups.*

(a) Linear slope in space

Number of spatial cells	Integral value	Logarithm of $\Delta\eta$ with respect to x
2^4	6.60039617181919	-
2^5	6.59313078772290	3.8422
2^6	6.59362237334188	4.7138
2^7	6.59359830208162	1.5822
2^8	6.59360416117280	5.1702
2^9	6.59360433170359	5.7244
2^{10}	6.59360432975846	1.3750
2^{12} (ref)	6.59360432853798	

(b) Constant slope in space

Number of spatial cells	Integral value	Logarithm of $\Delta\eta$ with respect to x
2^4	6.60519125890965	-
2^5	6.59378074254466	6.0408
2^6	6.59336205141948	-0.4637
2^7	6.59365146574873	2.3773
2^8	6.59357939721423	0.8814
2^9	6.59359380347370	1.2113
2^{10}	6.59360294087865	2.5942
2^{12} (ref)	6.59360475438764	

B.2. Energy plateau as boundary condition

Table B.3: $\log \Delta\eta$ *as function of* ΔE *for different amounts of energy groups with an energy plateau on the inlet. The exact values of the double integrals over space and energy are also given. Data is generated using 128 spatial elements*

(a) Linear slope in space

Number of groups	Integral value	Logarithm of $\Delta\eta$ with respect to E
2^4	121061827.837649	-
2^5	122218719.475643	1.9695
2^6	122506209.642963	2.0150
2^7	122576929.499933	2.0222
2^8	122594392.691565	2.0203
2^9	122598726.777619	2.0238
2^{10}	122599806.078983	2.0598
2^{12} (ref)	122600142.634392	

(b) Constant slope in space

Number of groups	Integral value	Logarithm of $\Delta\eta$ with respect to E
2^4	121065105.481811	-
2^5	122219590.032461	2.0121
2^6	122506453.259529	2.0221
2^7	122577004.871458	2.0176
2^8	122594418.526856	2.0150
2^9	122598736.717686	2.0248
2^{10}	122599810.302562	2.0778
2^{12} (ref)	122600143.550123	

Table B.4: $\log \Delta\eta$ *as function of* Δx *for different amounts of spatial cells with an energy plateau on the inlet. The exact values of the double integrals over space and energy are also given. Data is generated using 128 energy groups.*

(a) Linear slope in space

Number of spatial cells	Integral value	Logarithm of $\Delta\eta$ with respect to x
2^4	122581532.429042	-
2^5	122577504.905070	2.9797
2^6	122576994.192926	2.9822
2^7	122576929.499947	2.9915
2^8	122576921.362026	2.9960
2^9	122576920.341491	3.0003
2^{10}	122576920.213743	3.0167
2^{12} (ref)	122576920.195733	

(b) Constant slope in space

Number of spatial cells	Integral value	Logarithm of $\Delta\eta$ with respect to x
2^4	122583722.416458	-
2^5	122578144.066039	2.4760
2^6	122577200.457745	2.1326
2^7	122577004.871445	1.7450
2^8	122576952.088479	1.4529
2^9	122576933.970827	1.3090
2^{10}	122576926.595237	1.3275
2^{12} (ref)	122576921.709908	

Bibliography

E. Anderson, Z. Bai, C. Bischof, S. Blackford, J. Demmel, J. Dongarra, J. Du Croz, A. Greenbaum, S. Hammarling, A. McKenney, and D. Sorensen. *LAPACK Users' Guide*. Society for Industrial and Applied Mathematics, third edition, 1999. ISBN 0-89871-447-8 (paperback).

Yousry Azmy and Enrico Sartori. *Nuclear Computational Science*. Springer Science + Business Media, 2010. doi: 10.1007/978-90-481-3411-3. URL http://dx.doi.org/10.1007/978-90-481-3411-3.

M.J. Berger, D.S. Zucker, M.A. Zucker, and Chang J. *ESTAR, PSTAR, and ASTAR: Computer Programs for Calculating Stopping-Power and Range Tables for Electrons, Protons, and Helium Ions*, 2005. URL http://physics.nist.gov/Star.

H.A. Bethe. Zur theorie des durchgangs schneller korpuskularstrahlen durch materie. *Ann. d. Physik*, 5(325), 1930.

E. Hamilton James J. Duderstadt, Duderstadt. *Nuclear Reactor Analysis*. JOHN WILEY & SONS INC, 1976. ISBN 0471223638. URL http://www.ebook.de/de/product/3597336/james_j_duderstadt_duderstadt_e_hamilton_nuclear_reactor_analysis.html.

Martin Jermann. Particle therapy statistics in 2014. *International Journal of Particle Therapy*, 2(1):50–54, jun 2015. doi: 10.14338/ijpt-15-00013. URL http://dx.doi.org/10.14338/IJPT-15-00013.

A. Kolmogoroff. Über die analytischen methoden in der wahrscheinlichkeitsrechnung. *Mathematische Annalen*, 104(1):415–458, dec 1931. doi: 10.1007/bf01457949. URL http://dx.doi.org/10.1007/BF01457949.

MATLAB. *version 9.0.0.307022 (R2016a)*. The MathWorks Inc., Natick, Massachusetts, 2016.

H. Paganetti et al. *Proton Therapy Physics*. Taylor & Francis Inc, 2011. ISBN 1439836442.

W.H. Press et al. *Numerical Recipes in Fortran 77*, volume 1. Cambridge University Press, second edition, 1992. ISBN 0-521-43064-X.

Proton Therapy Center. Depth distribution of energy for protons and photons, 2012. URL http://www.proton-cancer-treatment.com/proton-therapy/principles-of-proton-therapy/.

S. Uilkema. Proton therapy planning using the S_N method with the fokker-planck approximation. Master's thesis, TU Delft, oct 2012.

J. van Kan, A. Segal, and F. Vermolen. *Numerical Methods in Scientific Computing*. VSSD, first edition, 2005. ISBN 90-71301-50-8.

Robert R. Wilson. Radiological use of fast protons. *Radiology*, 47(5):487–491, nov 1946. doi: 10.1148/47.5.487. URL http://dx.doi.org/10.1148/47.5.487.